

## Supplementary Information

# Energy Harnessing and Storage from Surface Switching with a Ferroelectric-Electrolyte

Maria Helena Braga

Engineering Physics Department, Engineering Faculty, University of Porto, 4200-465 Porto, Portugal

LAETA - INEGI, Institute of Science and Innovation in Mechanical and Industrial Engineering, 4200-465 Porto, Portugal

MatER, Materials for Energy Research, Engineering Faculty, University of Porto, 4200-465 Porto, Portugal  
correspondence to: mbraga@fe.up.pt

### 1. Introduction

The Belousov-Zhabotinsky (BZ) reaction is a classic example of a non-equilibrium chemical oscillator that displays positive feedback mechanisms and periodic behavior<sup>1</sup>. This reaction is one of the most famous examples of a nonlinear chemical oscillator<sup>2,3</sup>, where the concentration of reactants periodically changes over time. It is an oscillating chemical reaction, typically involving a mixture of potassium bromate, malonic acid, and cerium(IV) sulfate in a sulfuric acid solution<sup>3</sup>. This chemical oscillator exemplifies complex, nonlinear dynamics where simple chemical reactions lead to periodic or chaotic behaviors due to feedback loops and kinetic interactions among the reactants. In electronics, it can be represented by an LC (inductor-capacitor) circuit with a nonlinear resistor. The nonlinear resistor is usually implemented using a combination of components like diodes, and transistors.

The van der Pol (vdP) oscillator<sup>4-7</sup> is a type of nonlinear oscillator used to create the necessary nonlinearity that mimics the self-oscillating behavior of the BZ reaction. Relaxation oscillators<sup>3</sup> such as Pearson-Anson oscillators, are described by vdP equivalent circuits and can also be used to model the BZ reaction. These circuits produce a waveform that alternates between two levels<sup>8</sup>, analogous to the concentration changes in the chemical oscillations of the BZ reaction. Using a Schmitt trigger<sup>9</sup>, a comparator circuit with hysteresis, can also help simulate the sudden transitions in BZ reaction oscillations.

In<sup>10</sup>, it was demonstrated vdP-Duffing Hodgkin-Huxley and FitzHugh-Nagumo oscillators<sup>6</sup> in electrochemical/electrostatic energy harvesting and storage cell architectures. Analogous to Rabi's oscillations arising from Floquet states, stationary solutions of a quantum system in the presence of a periodic time-dependent perturbation were studied<sup>10</sup>. These time-dependent forced oscillations are introduced herein by an association of Josephson junctions (JJ) in series corresponding to higher-frequency displaced oscillators acting at the surface and inducing

synchronized-lower frequency bulk oscillations. The latter is supported by a non-linear negative resistance<sup>11</sup>.

A ferroelectric topologic insulator FETI<sup>12–16</sup> is a ferroelectric and, therefore, a dielectric material with the capability to polarize spontaneously and to reverse that polarization with the application of an external electrical field and a topological insulator TI with the presence of conducting states on the surface, which are protected by the material's topological nature and spin-momentum locking. These surface states are robust and not easily disrupted by impurities or imperfections in the material, making them potentially useful for various electronics and quantum computing applications. The FETIs introduced herein<sup>12–19</sup> display two oscillation levels corresponding to surface and surface–bulk synchronization.

It is noteworthy that all the self-oscillation features demonstrated with the FETI-electrolytes of the  $A_{3-2x}Ba_xClO$  family (where  $A = Na$  or  $K$ , and  $x = 0$  or  $0.005$ ) and their conductor<sub>1</sub>/ $A_{3-2x}Ba_xClO$ /conductor<sub>2</sub> cells, where conductor<sub>1</sub> = Al, Zn and conductor<sub>2</sub> = Cu, C, with double layer or coaxial geometries, are well described by the same equivalent circuit that describes what seemed to be, a priori, unrelated systems such as BZ reactions and topoelectrical circuits. Self-oscillation features in FETIs are found in **(1)** chemical potential leading to self-charge, **(2)** thermal (pyro), and **(3)** piezoelectric outputs.

All this panoply of self-charge and self-oscillation possibilities may be excited at a steady temperature and a relatively constant potential difference, even while set to discharge with load. While challenging to ‘tame,’ self-charge and self-oscillations have an almost inexorable number of applications in energy-related technologies (harvesting and storage) beyond sensors, actuators, catalysts, memories, data transmission, and transistors. Therefore, FETIs have become the hope for achieving energy-efficient harvesting, storage, and switching<sup>12</sup>.

The electrical equivalent circuit introduced herein to describe the FETI as a sample or performing in an electrochemical cell is similar to the Kotwal et al.<sup>20</sup> circuits introduced to simulate active top electrical material circuits. However, in our case, the surface oscillations are JJ, highlighting the quantum character of the oscillations that show Floquet-thermal<sup>21–24</sup> and piezoelectric<sup>25–29</sup> phenomena.

TI states have been documented and observed in various materials. Instances of such behavior include the demonstration of a non-trivial topological insulator phase in halide perovskite<sup>12,30</sup>, the identification of an oxide topological insulator derived from the superconductor  $BaBiO_3$ <sup>31</sup>, and the discovery of a topological phase in the non-centrosymmetric material  $NaSnBi$ <sup>32</sup>.

In their 2016 theoretical analysis, Liu et al.<sup>13</sup> examined the cubic halide perovskite  $CsPbI_3$ , investigating the implications of simultaneous ferroelectricity and nontrivial topological

properties. This particular cubic halide perovskite transitions from a paraelectric to a ferroelectric structural phase when subjected to strain. Applying pressure to CsPbI<sub>3</sub> can induce a shift from its standard insulating state to a topological insulating phase. FETIs<sup>13-19</sup> represent a significant improvement over conventional Ferroelectric Normal Insulators (FENIs)<sup>12</sup> because they inherently possess metallic surface states. These states can function like integrated metallic electrodes, promoting an inherent short-circuit condition that aids in the automatic dispersal of surface charge and enables self-charging mechanisms within the device. Therefore, FETIs could act as combined dielectric-electrode systems, reducing interface resistance and potentially being used as single-electrode components in batteries or capacitors to maximize the potential bias.

One of the significant challenges with FETIs, similar to many other advanced materials, is their temperature sensitivity. While not all FETIs are limited to low-temperature operations, the stability of their ferroelectric and topological properties can be significantly influenced by temperature. In some cases, the desired ferroelectric or topological characteristics are only observable at low temperatures, limiting their practical applications at room temperature.

The synthesis and fabrication of high-quality FETI materials can be challenging. Defects, impurities, and structural irregularities can significantly affect their properties on the ferroelectric side. Achieving a perfect or near-perfect crystal structure is often necessary for these materials to exhibit the desired properties, which can be difficult and expensive.

Another challenge is the scalability of FETI materials for practical applications. Manufacturing these materials on a large scale while maintaining their unique properties is not straightforward; it takes effort, and integrating them into existing electronic and spintronic devices poses additional challenges, particularly in compatibility with other materials and fabrication processes.

These latter reasons likely explain that besides the studies on 2D FETI such as Bi<sub>2</sub>Te<sub>3</sub><sup>18</sup> and In<sub>2</sub>Se<sub>3</sub><sup>33</sup>, there are mainly only theoretical studies on FETI, while the few materials studied experimentally were performed at low temperatures<sup>19</sup>. Herein, we show recurring to experiments and simulations, a ferroelectric-electrolyte family (A<sub>2.99</sub>Ba<sub>0.005</sub>ClO; A = Na and K) with topologic insulator behavior enhanced at approximately their glass transition (33 – 63 °C).

## 2. Materials and Methods

### **Synthesis of $\text{Na}_{2.99}\text{Ba}_{0.005}\text{ClO}$ FETI-electrolyte, fabrication, and cycling of the $\text{Zn}/\text{Na}_{2.99}\text{Ba}_{0.005}\text{ClO}/\text{Cu}$ battery pouch cell (Fig. 1)**

The electrolyte  $\text{Na}_{2.99}\text{Ba}_{0.005}\text{Cl}_{1-x}\text{O}(\text{OH})_x$  was produced starting from high-purity raw materials: NaCl (with a purity of 99.5%, sourced from ITW Reagents, PanReac AppliChem), Na(OH) (98.0% pure, provided by LabKem), and Ba(OH)<sub>2</sub> (anhydrous form, purity ranging from 94 to 98%, obtained from Alfa Aesar). The preparation process involved allowing these components to react in deionized water in a teflon reactor and subsequently dry at temperatures between 230 and 250 °C. Once the  $\text{Na}_{2.99}\text{Ba}_{0.005}\text{ClO}$  solid-state material was formed, it was subjected to a grinding process. This was done for 40 minutes at 300 rpm in a ball milling machine equipped with an Agate container and five 20 mm diameter balls. The container was designed to be airtight to prevent moisture absorption, as mentioned in a previous study.

The study further explored the use of  $\text{Na}_{2.99}\text{Ba}_{0.005}\text{ClO}$  in double-layer pouch cells, specifically  $\text{Zn}/\text{Na}_{2.99}\text{Ba}_{0.005}\text{ClO}/\text{Cu}$  cells. The negative electrode consisted of a zinc (Zn) sheet with  $2.5 \times 2.5 = 6.25 \text{ cm}^2$  and thickness 0.5 mm; the positive electrode consisted of a carbon-felt with  $4.00 \text{ cm}^2$ , 1 mm thick, in contact with a sheet of copper (Cu) with  $6.25 \text{ cm}^2$ , 0.3 mm thick. The electrode edges were protected by Teflon tape to avoid short circuits, reducing the electrodes' effective surface area. The electrodes were separated by a layer of  $\text{Na}_{2.99}\text{Ba}_{0.005}\text{ClO}$  FETI-electrolyte composite with a mixture of 80 wt.%  $\text{Na}_{2.99}\text{Ba}_{0.005}\text{ClO}$  + 20 wt.% PVAc. The PVAc is a binder and allows a better contact with the electrodes. The cell was pressed (unidirectional) at  $0.46 \text{ kgf.cm}^{-2}$  for 20 min at room temperature during fabrication. The effective surface area is finally  $\sim 2.30 \text{ cm}^2$ , and the thickness  $\sim 4 \text{ mm}$ . The carbon felt becomes a thin layer with  $< 0.2 \text{ mm}$  after being pressed.

The electrochemical cycling was performed using a potentiostat Biologic SP240. The resistance of the external resistors was verified using an ohmmeter. The cell was heated in a sandbox, and subsequently kept at a constant temperature.

### **Differential equations ODE system (Fig. 1)**

The differential equation in Eq. (1) results from the equivalent circuit in Fig. 1c. The correspondent simulated dynamical system in Fig. 1d were solved using the Runge-Kutta 4<sup>th</sup>-order numerical method and a code implemented at wxMaxima 20.06.6 (ref. <sup>34</sup>).

### **Density functional theory (DFT) and *ab initio* molecular dynamics (AMD) (Fig. 1)**

In the realm of computational analysis, the study employed Density Functional Theory (DFT) and Ab initio Molecular Dynamics (AMD), facilitated by the VASP<sup>35</sup> software. Simulations were focused on a  $(\text{Na}_3\text{ClO})_{27}$  supercell, maintained at 37 °C (310 K). The initial structure, set at 37 °C, was

derived from microcanonical NV'E simulations on a supercell with a triclinic P1 crystal structure, initially optimized from a cubic Pm-3m (antiperovskite structure).

AMD simulations were carried out in two environments: (1) a canonical NV'T ensemble using Nosé's thermostat<sup>36</sup> with 4 fs time steps up to 8 ps, where velocities were adjusted to maintain constant temperature, and (2) an isothermal-isobaric NP'T ensemble. The DFT simulations utilized projector augmented wave (PAW) potentials within the generalized gradient approximation (GGA) framework<sup>37</sup>. Electronic structure calculations were performed with a cut-off energy of 500 eV, and a k-spacing of  $0.25 \text{ \AA}^{-1}$ , resulting in a  $2 \times 2 \times 2$  mesh.

From the 37 °C supercell, a cube was built with a 13 Å vacuum layer in all 3D to disrupt periodicity. The electron localization functions (ELF) were computed for a (001) surface. For these calculations, tools from VASP and Electronics within the MedeA 3.6 software<sup>38</sup> were utilized, as referenced in previous studies.

### **Poincaré maps (Figs. 1 to 3)**

The Poincaré maps were obtained using the Origin Pro app<sup>39</sup> and the experimental data plotted in phase portraits.

### **Synthesis of $\text{K}_{2.99}\text{Ba}_{0.005}\text{ClO}$ and Al/ $\text{K}_{2.99}\text{Ba}_{0.005}\text{ClO}$ /Cu (mesh) coaxial battery cell (Fig. 2)**

The synthesis of  $\text{K}_{2.99}\text{Ba}_{0.005}\text{ClO}$  and the fabrication of Al/ $\text{K}_{2.99}\text{Ba}_{0.005}\text{ClO}$ /Cu (mesh) coaxial battery cell were described previously in<sup>40</sup>. The electrochemical cycles consisting of charge for 3 min at 1.3 V followed by a discharge for 24 h with a  $R_{ext} = 1.8 \text{ } \Omega$ . The sample consistently shows self-charge and self-cycling while set to discharge with the resistor of  $1.8 \text{ } \Omega$ <sup>12</sup>.

### **Temperature-modulated differential scanning calorimetry (MDSC) and thermogravimetry analysis (TGA) (Fig. 3)**

For this study, differential scanning calorimetry (DSC) was conducted using the Discover 25 model from TA Instruments. This equipment states a temperature accuracy of  $\pm 0.1 \text{ } ^\circ\text{C}$  and a precision of  $\pm 0.01 \text{ } ^\circ\text{C}$ . Before conducting the experiments, a calibration process was undertaken. Initially, indium was utilized in the sample crucible for calibration, covering a temperature range from  $-39.7$  to  $250.4 \text{ } ^\circ\text{C}$  at a heating rate of  $20.0 \text{ } ^\circ\text{C}\cdot\text{min}^{-1}$ . Subsequently, sapphire calibration was performed within a range of  $0.00$  to  $237.61 \text{ } ^\circ\text{C}$  at  $3.00 \text{ } ^\circ\text{C}\cdot\text{min}^{-1}$ . Alumina crucibles were consistently used for these calibrations. Nitrogen gas was employed as the purge gas at a  $50 \text{ mL}\cdot\text{min}^{-1}$  flow rate.

In addition to DSC, thermogravimetric analysis (TGA) was carried out using the TGA 550 model (Fig. 3a), also from TA Instruments. This analysis aimed to observe changes in the mass of the samples with temperature and time. The TGA calibration and experiments were conducted over a

temperature range from ambient up to 260 °C, with a heating rate of 5 °C.min<sup>-1</sup>. The small difference in rates of the DSC and TGA experiments can account for a certain displacement in the glass transition  $T_g$  in Fig. 3g. The samples were placed in alumina crucibles on a platinum pan (100  $\mu$ L). Like in DSC, nitrogen was the chosen gas for TGA, but with a flow rate of 100 mL.min<sup>-1</sup>. Both the MDSC and TGA experiments were performed with sample weights not exceeding 15 mg. The TGA sample had a thickness of  $\sim 1.6$  mm and a surface area  $A \approx 2.6$  mm<sup>2</sup>.

### 3. Supplementary Figures

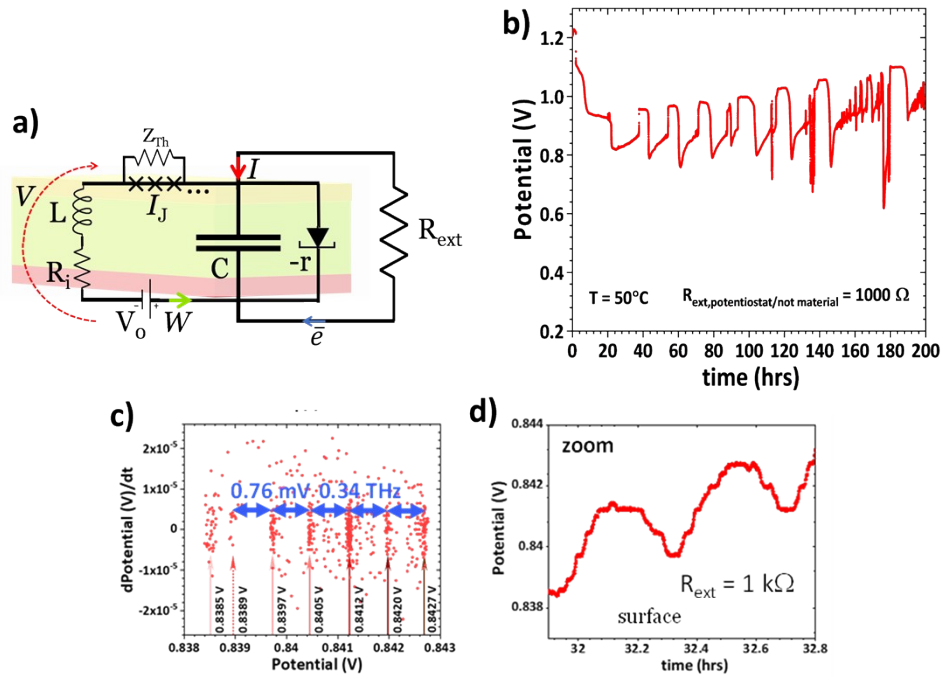


**Figure S1.** **a** Equivalent circuit that simulates the Zn/Na<sub>2.99</sub>Ba<sub>0.005</sub>ClO (FETI)/Cu battery cell; **b** potential vs time for the Zn/Na<sub>2.99</sub>Ba<sub>0.005</sub>ClO FETI/Cu battery cell when set to discharge with a 1000  $\Omega$  resistor at 50 °C showing self-charge and fractal features; **c** phase portrait of the zoom of **b** shown in **d**.

$$\begin{cases} \dot{V} = \frac{V}{R_{ext}} - F(V) - W \\ \dot{W} = \frac{C}{V + V_0 - R_i W - Z_{Th} I_J} \\ \dot{\phi} = aW \end{cases} \quad \text{where}$$

The ODE system corresponds to the equivalent circuit in Fig. S1a  $V$  is the potential difference in the terminals of the cell or external resistor;  $W$  the current on the inductor's branch;  $V_0$  is the source voltage due to the initial chemical potential difference between

the electrodes;  $R_i$  is the internal resistance,  $L$  is the inductor due to the kinetic behavior at a specific absolute temperature,  $Z_{Th}$  is the Thévenin or Norton equivalent impedance for the array of JJ associated in series;  $I_J$  is the Josephson current equivalent in the absence of a magnetic field,  $C$  is the capacitor constituted by two conductors Zn and Cu separated by the  $\text{Na}_{2.99}\text{Ba}_{0.005}\text{ClO}$  (FETI), and  $-r(V)$  is the negative nonlinear resistance of the tunnel diode branch is a polynomial function of the potential  $F(V)$  of the ferroelectric nonlinear behavior, obtained experimentally from the I-V plot through cyclic voltammetry. The phase  $\phi$  is related to the chemical potential difference across

the JJ,  $\Delta\mu = 2e\Delta V$ , of potential difference  $\Delta V$ ,  $\dot{\phi} = -\frac{\Delta\mu}{\hbar} = -2e\frac{\Delta V}{\hbar} = aW$ ;  $2e$  is the electrical charge corresponding to a Cooper pair (boson)<sup>41</sup>, and  $a$  a parameter. It is noteworthy to highlight that the phase variation across the JJ leading to an alternate current, is owing to differences in chemical potentials across the atomic plans due to an uneven distribution of the electrons across the plans at the surface.

A JJ under a chemical potential  $\Delta\mu$  drive is periodically actuated. As a result, the junction dynamics can be analyzed using Floquet theory, where the Shapiro steps can be understood as resonances between the AC driving frequency and the natural oscillation frequency of the Cooper pairs in the junction (Josephson frequency). These resonances lead to the stabilization of certain voltage states (the Shapiro steps) (Fig. S1c-d zoom). The Floquet thermal states help in describing the energy distribution and dynamics of the system in a nonequilibrium, periodically driven regime. Floquet's theory predicts that energy can be absorbed from the driving field into the quantum system, leading the system's energy levels to change over time. This energy absorption from the periodic potential is referred to as Floquet heating.

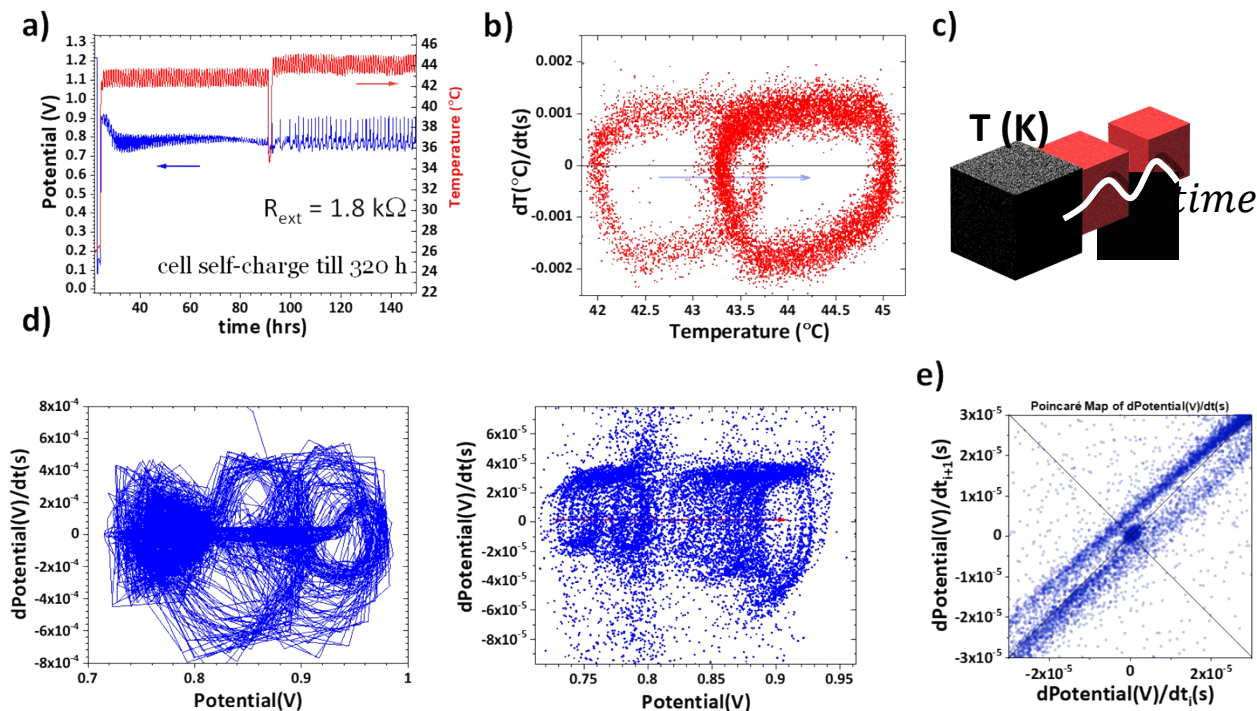


**Figure S2.** Electrochemical and thermal (pyro) self-cycling of an Al/ $K_{2.99}Ba_{0.005}ClO$  composite/Cu (mesh) coaxial structural battery<sup>40</sup>; **a** set to discharge with a 1.8 k $\Omega$  resistor at  $\sim 25$  °C for 22.8 h, and then heated to  $\sim 42.5$  °C remaining at this temperature for 320 h<sup>40</sup>; only 150 h are shown for a detailed analysis; **b** phase portrait of the self-cycling temperature in **a** showing two limit cycles, with the focus on (42.8 °C,  $-2.48 \times 10^{-4}$  °C.s<sup>-1</sup>) and (44.2 °C,  $-2.48 \times 10^{-4}$  °C.s<sup>-1</sup>) that interconnect, meaning that even after a quick disruption on the steady external temperature, the amplitude of the temperature oscillations and the amplitude of the temperature rate do not vary; both temperatures highlight the protected states; the phase portrait shows Floquet states where a quantum-classical correspondence holds coherent such as the illustration attempts to describe in **c**; **d** shows the phase portrait (left) for the potential difference in **a**, and its zoom (right) corresponding to the surface displaced self-oscillations based on JJ in AC; in **e** the corresponding Poincaré map that does not show a lattice of periodic points, conversely to the corresponding temperature in **b**.

## X-ray diffraction

The XRD patterns for different temperatures from 24 to 230 °C. Figure S3 shows the small angle XRD, with the amorphous  $Na_{2.99}Ba_{0.005}ClO$  and  $K_{2.99}Ba_{0.005}ClO$  corresponding to the “bump” in the background for  $7^\circ \leq 2\theta \leq 25^\circ$  and the unequivocal presence of NaCl in excess (Figs. S3a and S3b), one of the precursors of the glass that reflects the x-ray radiation intensely. At 230 °C, NaCl and NaOH have the same initial wt.%, but  $Na_{2.99}Ba_{0.005}ClO$  (crystalline) forms from the equivalent hydride phases. If the XRD had been performed in a capillary with no excess precursors, all the precursors would have reacted. An amorphous product could have been observed at 250 °C, even in a synchrotron experiment. The NaCl and NaOH phase diagrams do not show any phase transitions corresponding to the ones observed herein. The relative intensities for  $Na_3ClO$ , NaCl, and NaOH were obtained with the Match! Software (Figs. S3a and S3b). It is highlighted that the analyzed sample was  $Na_{2.99}Ba_{0.005}ClO$  and not  $Na_3ClO$ , which affects the diffraction pattern.

The  $K_{2.99}Ba_{0.005}ClO$  diffraction pattern at 48 °C shows an amorphous phase, as mentioned, and a crystalline phase that is shifted to smaller angles  $\approx 5^\circ$  ( $2\theta$ ), compared to  $Na_{2.99}Ba_{0.005}ClO$ , which is likely slightly distorted to tetragonal from the cubic structure, Pm-3m. Rietveld refinement is still lacking; however, the amorphous phase is the one that enhances the properties of the ferroelectric.

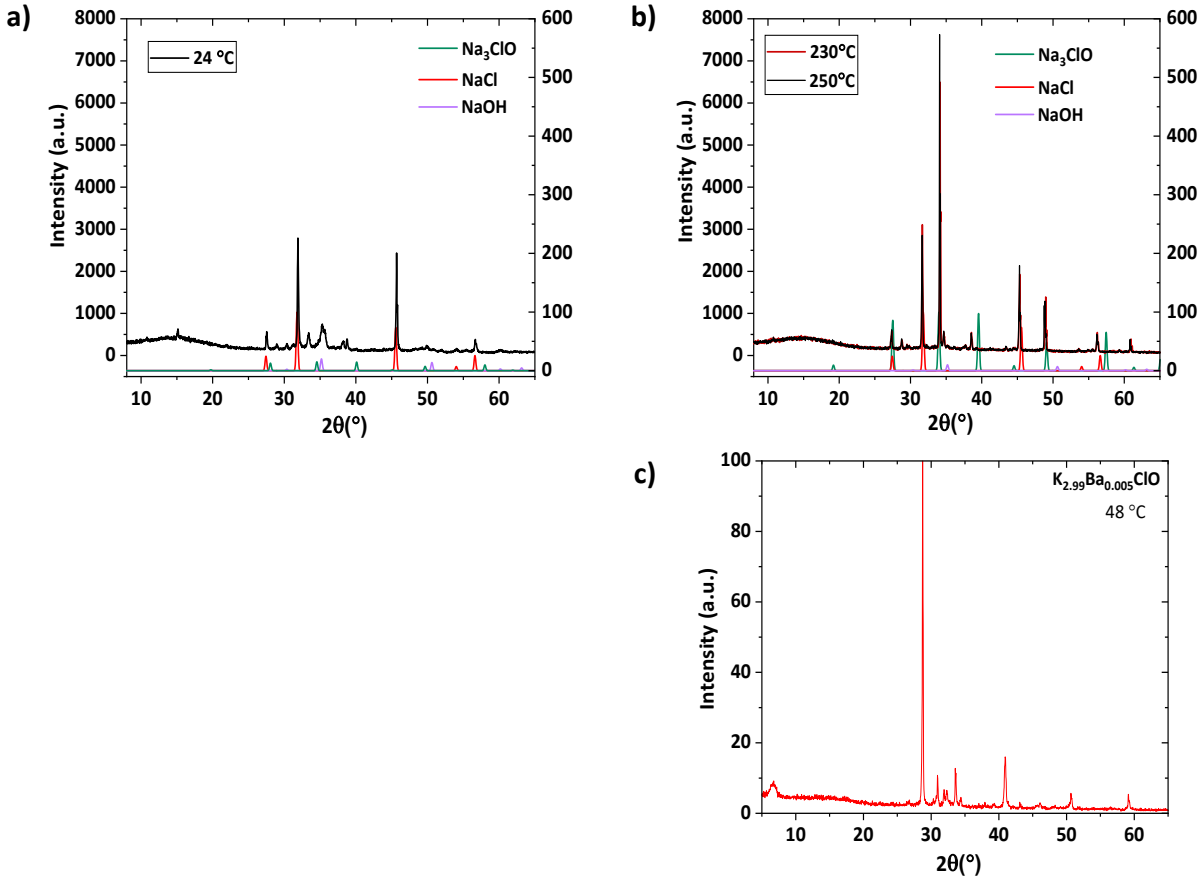


**Figure S3.** X-ray diffraction at **a)** 24 °C, mainly showing the relative intensities of NaCl and the background “bump”  $7^\circ \leq 2\theta \leq 25^\circ$  corresponding to the amorphous  $Na_{2.99}Ba_{0.005}ClO$ ; **b)** 230 and 250 °C, showing the relative intensities of the detected phases ( $Na_3ClO$  and  $NaCl$ ) and the background “bump” corresponding to the amorphous  $Na_{2.99}Ba_{0.005}ClO$ ; At 230 °C, the hydroxide phases release water while forming  $Na_{2.99}Ba_{0.005}ClO$  (crystalline). It is noteworthy to highlight that the  $NaCl$  reflects the  $CuK\alpha$  electromagnetic radiation intensely. The relative amounts of the crystalline phases are proportional to the intensities except for the amorphous phase. **c)** X-ray diffraction at 48°C, showing the background “bump”  $7^\circ \leq 2\theta \leq 25^\circ$  corresponding to the amorphous  $K_{2.99}Ba_{0.005}ClO$  and its crystalline phase that is likely shifted  $5^\circ$  ( $2\theta$ ) toward small angles from  $Na_{2.99}Ba_{0.005}ClO$ .

## References

- 1 L. Howell, E. Osborne, A. Franklin and É. Hébrard, *J. Phys. Chem. B*, 2021, **125**, 1667–  
1673.
- 2 C. Zhai, A. Palazoglu and W. Sun, *IFAC-PapersOnLine*, 2018, **51**, 738–743.
- 3 A. Cassani, A. Monteverde and M. Piumetti, *J Math Chem*, 2021, **59**, 792–826.
- 4 F. Stumpers, *IRE Transactions on Circuit Theory*, 1960, **7**, 366–367.
- 5 G. Israel, in *Technological Concepts and Mathematical Models in the Evolution of  
Modern Engineering Systems: Controlling • Managing • Organizing*, eds. A. M. Gasca,  
M. Lucertini and F. Nicolò, Birkhäuser, Basel, 2004, pp. 52–77.
- 6 M. Tsatsos, 2008.
- 7 Van der Pol model in two-delay differential equation representation | Scientific Reports,  
<https://www.nature.com/articles/s41598-022-06911-3>, (accessed 1 January 2024).
- 8 C. Otto, B. Lingnau, E. Schöll and K. Lüdge, *Opt. Express, OE*, 2014, **22**, 13288–13307.
- 9 Y. Kato and H. Nakao, *New J. Phys.*, 2021, **23**, 043018.
- 10 M. H. Braga, *Materials*, 2021, **14**, 2398.
- 11 M. H. Braga, J. E. Oliveira, A. J. Murchison and J. B. Goodenough, *Applied Physics  
Reviews*, 2020, **7**, 011406.
- 12 B. M. Gomes, J. F. R. Moutinho and M. H. Braga, *J. Mater. Chem. A*, 2024, **12**, 690–722.
- 13 S. Liu, Y. Kim, L. Z. Tan and A. M. Rappe, *Nano Lett.*, 2016, **16**, 1663–1668.
- 14 H. Bai, X. Wang, W. Wu, P. He, Z. Xu, S. A. Yang and Y. Lu, *Phys. Rev. B*, 2020, **102**,  
235403.
- 15 M. Wu and J. Li, *Proceedings of the National Academy of Sciences*, 2021, **118**,  
e2115703118.
- 16 A. Marrazzo and M. Gibertini, *npj 2D Mater Appl*, 2022, **6**, 1–10.
- 17 N. Mao, R. Li, X. Zou, Y. Dai, B. Huang and C. Niu, *Phys. Rev. B*, 2023, **107**, 045125.
- 18 Y. Liang, N. Mao, Y. Dai, L. Kou, B. Huang and Y. Ma, *npj Comput Mater*, 2021, **7**, 1–6.
- 19 H. Takahashi, T. Sasaki, A. Nakano, K. Akiba, M. Takahashi, A. H. Mayo, M. Onose, T. C.  
Kobayashi and S. Ishiwata, *npj Quantum Mater.*, 2023, **8**, 1–7.
- 20 Active topoelectrical circuits | PNAS,  
<https://www.pnas.org/doi/full/10.1073/pnas.2106411118>, (accessed 1 January 2024).
- 21 Z. Song and L.-W. Wang, *npj Quantum Mater.*, 2020, **5**, 1–7.
- 22 M. S. Rudner and N. H. Lindner, *Nat Rev Phys*, 2020, **2**, 229–244.
- 23 N. Gupt, S. Bhattacharyya, B. Das, S. Datta, V. Mukherjee and A. Ghosh, *Phys. Rev. E*,  
2022, **106**, 024110.
- 24 Phys. Rev. X 10, 021044 (2020) - Floquet Prethermalization in a Bose-Hubbard System,  
<https://journals.aps.org/prx/abstract/10.1103/PhysRevX.10.021044>, (accessed 7 January  
2024).
- 25 L. Zhao, M. D. K. Lee, M. M. Aliyu and H. Loh, *Nat Commun*, 2023, **14**, 7128.
- 26 R. Fleury, A. B. Khanikaev and A. Alù, *Nat Commun*, 2016, **7**, 11744.
- 27 A. Darabi, X. Ni, M. Leamy and A. Alù, *Science Advances*, 2020, **6**, eaba8656.
- 28 C. Xu, P. Wei, Z. Wei and X. Guo, *Thin-Walled Structures*, 2023, **191**, 111059.
- 29 S. Yin, E. Galiffi and A. Alù, *eLight*, 2022, **2**, 8.
- 30 H. Jin, J. Im and A. J. Freeman, *Phys. Rev. B*, 2012, **86**, 121102.
- 31 B. Yan, M. Jansen and C. Felser, *Nature Phys*, 2013, **9**, 709–711.
- 32 X. Dai, C.-C. Le, X.-X. Wu, S.-S. Qin, Z.-P. Lin and J.-P. Hu, *Chinese Phys. Lett.*, 2016, **33**,  
127301.
- 33 C. Wang, L. You, D. Cobden and J. Wang, *Nat. Mater.*, 2023, **22**, 542–552.
- 34 wxMaxima, <https://wxmaxima-developers.github.io/wxmaxima/index.html>, (accessed 13  
January 2024).
- 35 G. Kresse and J. Furthmüller, *Phys. Rev. B*, 1996, **54**, 11169–11186.
- 36 N. Shuichi, *Progress of Theoretical Physics Supplement*, 1991, **103**, 1–46.
- 37 J. P. Perdew and Y. Wang, *Phys. Rev. B*, 1992, **45**, 13244–13249.

- 38 Products, <https://www.materialsdesign.com/products>, (accessed 13 January 2024).
- 39 Poincare Plot - File Exchange - OriginLab,  
<https://www.originlab.com/fileExchange/details.aspx?fid=404>, (accessed 13 January 2024).
- 40 F. Danzi, M. Valente, S. Terlicka and M. H. Braga, *APL Materials*, 2022, **10**, 031111.
- 41 B. Pal, A. Chakraborty, P. K. Sivakumar, M. Davydova, A. K. Gopi, A. K. Pandeya, J. A. Krieger, Y. Zhang, M. Date, S. Ju, N. Yuan, N. B. M. Schröter, L. Fu and S. S. P. Parkin, *Nat. Phys.*, 2022, **18**, 1228–1233.